

Evolution at $z \gtrsim 0.5$ of the X-ray properties of simulated galaxy clusters: comparison with the observational constraints

S. Ettori¹, S. Borgani^{2,3}, L. Moscardini⁴, G. Murante⁵, P. Tozzi⁶,
A. Diaferio⁷, K. Dolag⁸, V. Springel⁹, G. Tormen⁸, L. Tornatore²

¹ ESO, Karl-Schwarzschild-Str. 2, D-85748 Garching, Germany (settori@eso.org)

² Dipartimento di Astronomia dell'Università di Trieste, via Tiepolo 11, I-34131 Trieste, Italy (borgani,tornatore@ts.astro.it)

³ INFN – National Institute for Nuclear Physics, Trieste, Italy

⁴ Dipartimento di Astronomia, Università di Bologna, via Ranzani 1, I-40127 Bologna, Italy (lauro.moscardini@unibo.it)

⁵ INAF, Osservatorio Astronomico di Torino, Strada Osservatorio 20, I-10025 Pino Torinese, Italy (murante@to.astro.it)

⁶ INAF, Osservatorio Astronomico di Trieste, via Tiepolo 11, I-34131 Trieste, Italy (tozzi@ts.astro.it)

⁷ Dipartimento di Fisica Generale “Amedeo Avogadro”, Università degli Studi di Torino, via Giuria 1, Torino, Italy (diaferio@ph.unito.it)

⁸ Dipartimento di Astronomia, Università di Padova, vicolo dell'Osservatorio 2, I-35122 Padova, Italy (kdolag,tormen@pd.astro.it)

⁹ Max-Planck-Institut für Astrophysik, Karl-Schwarzschild Strasse 1, Garching bei München, Germany (volker@mpa-garching.mpg.de)

submitted on 23 Feb 04; accepted on 1 Jul 04

ABSTRACT

We analyze the X-ray properties of a sample of local and high redshift galaxy clusters extracted from a large cosmological hydrodynamical simulation. This simulation has been realized using the Tree+SPH code GADGET-2 for a Λ CDM model. It includes radiative cooling, star formation and supernova feedback and allows to resolve radially the thermodynamic structure of clusters up to redshift 1 in a way that is not yet completely accessible to observations. We consider only objects with $T_{\text{ew}} > 2$ keV to avoid the large scatter in the physical properties present at the scale of groups and compare their properties to recent observational constraints. In our analysis, we adopt an approach that mimics observations, associating with each measurement an error comparable with recent observations and providing best-fit results via robust techniques. Within the clusters, baryons are distributed among (i) a cold neutral phase, with a relative contribution that increases from less than 1 to 3 per cent at higher redshift, (ii) stars which contribute with about 20 per cent and (iii) the X-ray emitting plasma that contributes by 80 (76) per cent at $z = 0$ (1) to the total baryonic budget. A depletion of the cosmic baryon fraction of ~ 7 (at $z = 0$) and 5 (at $z = 1$) per cent is measured at the virial radius, R_{vir} , in good agreement with adiabatic hydrodynamical simulations. We confirm that, also at redshift > 0.5 , power-law relations hold between gas temperature, T , bolometric luminosity, L , central entropy, S , gas mass, M_{gas} , and total gravitating mass, M_{tot} and that these relations are steeper than predicted by simple gravitational collapse. A significant, negative evolution in the $L - T$ and $L - M_{\text{tot}}$ relations and positive evolution in the $S - T$ relation are detected at $0.5 < z < 1$ in this set of simulated galaxy clusters. This is partially consistent with recent analyses of the observed properties of $z \gtrsim 0.5$ X-ray galaxy clusters. By fixing the slope to the values predicted by simple gravitational collapse, we measure at high redshift normalizations lower by 10–40 per cent in the $L - T$, $M_{\text{tot}} - T$, $M_{\text{gas}} - T$, $f_{\text{gas}} - T$ and $L - M_{\text{tot}}$ relations than the observed estimates. This suggests that either the amount of hot X-ray emitting plasma measured in the central regions of simulated systems is smaller than the observed one or a systematic higher value than actually measured of gas temperatures and total masses is recovered in the present simulated dataset.

Key words: cosmology: miscellaneous – methods: numerical – galaxies: cluster: general – X-ray: galaxies.

1 INTRODUCTION

Only in the recent years, and after deep exposures obtained through the new generation of X-ray telescopes like *Chandra* and *XMM-*

Newton, it has been possible to start investigating systematically the physical properties of galaxy clusters, at redshift higher than 0.4 (e.g. Holden et al. 2002, Vikhlinin et al. 2002, Ettori et al. 2004).

Galaxy clusters are believed to form under the action of the dark matter gravity in the hierarchical scenario of cosmic structure formation. They assemble cosmic baryons from the field and heat them up through adiabatic compression and shocks that take place during the dark matter halo collapse and accretion. Simple self-similar relations between the physical properties in clusters are then predicted (e.g. Kaiser 1986, 1991, Evrard & Henry 1991) since the gravity does not have any preferred scale and the hydrostatic equilibrium between X-ray (mostly originated through bremsstrahlung processes) emitting gas and the cluster potential is a reasonable assumption. Therefore, how the baryons distribute within the cluster potential as function of cosmological time and whether or not scaling relations between integrated physical properties still hold and, possibly, evolve at high redshift, these are fundamental diagnostics to validate the self-similar scenario and to study the formation and evolution of X-ray galaxy clusters. A main role in assessing these issues is played by cosmological hydrodynamical simulations that can drive the analysis of observationally unresolved high redshift systems.

To this purpose, we have analysed the predictions obtained at high redshift from the large hydrodynamical cosmological simulation presented and discussed in Borgani et al. (2004, hereafter Paper I), that has been shown to reproduce at $z = 0$ several observed properties of X-ray clusters, such as the local temperature function, the luminosity–temperature relation for systems hotter than 2 keV, and the mass–temperature relation.

As a natural follow-up of that work, we study here the evolution of the X-ray properties of the simulated galaxy clusters from $z = 0$ out to $z = 1$. This paper is organized as follows: in the next section, we describe our dataset of simulated clusters and their physical properties; in Section 3 we discuss how the baryons, and particularly the X-ray emitting plasma, are distributed in the local and $z \geq 0.5$ systems. In Section 4, we introduce the X-ray scaling relations and discuss their evolution at redshift 0.5–1 with a direct comparison with the observational results. Finally, we summarize and discuss our results in Section 5.

2 PROPERTIES OF THE SIMULATED CLUSTERS

The simulated clusters are extracted from the large-scale hydrodynamical simulations described in Paper I. We refer to that paper for a detailed description of the simulation, while we provide here only a short summary. The simulated cosmological model is a standard flat Λ CDM universe, with $\Omega_m = 1 - \Omega_\Lambda = 0.3$, $\sigma_8 = 0.8$, $\Omega_b h^2 = 0.019$ and $H_0 = 100h \text{ km s}^{-1} \text{ Mpc}^{-1}$ with $h = 0.7$. The simulation follows the evolution of 480^3 dark matters and an initially equal number of gas particles within a box of $192 h^{-1} \text{ Mpc}$ on a side, so that $m_{\text{DM}} = 6.6 \times 10^9 M_\odot$ and $m_{\text{gas}} = 9.9 \times 10^8 M_\odot$ for the mass of the DM and gas particles, respectively. The Plummer–equivalent gravitational softening of the simulation was set to $\epsilon_{\text{P1}} = 7.5 h^{-1} \text{ kpc}$ comoving from $z = 2$ to $z = 0$, while it was taken to be fixed in physical units at higher redshift.

The run has been realized using GADGET-2¹, a massively parallel tree N-body/SPH code (Springel, Yoshida & White 2001)

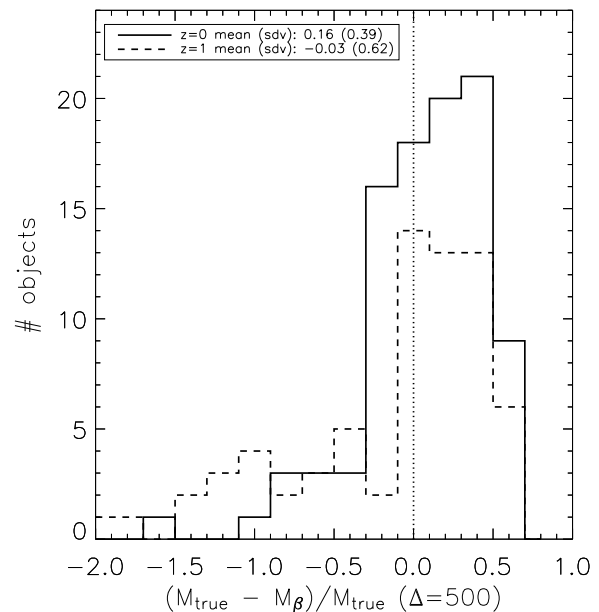


Figure 1. Comparison between the true cluster masses and estimates measured by using an isothermal β -model. Mean deviations of about 15 per cent (at $z = 0$) or less (at $z = 1$) are obtained.

with fully adaptive time-step integration, which includes the explicit energy and entropy conserving SPH formulation by Springel & Hernquist (2002). The simulation includes radiative cooling of a plasma of primordial composition, the effect of a photoionizing, time-dependent, uniform UV background (e.g., Haardt & Madau 1999). Star formation is treated using the self-regulated hybrid multiphase model for the interstellar medium introduced by Springel & Hernquist (2003). The code also includes a phenomenological description of galactic winds powered by type-II supernovae, such that star-forming gas particles contribute to the wind with a mass outflow rate two times larger than their star formation rate, with a wind velocity of about 360 km s^{-1} .

Clusters are identified in the simulation box by first applying a friends-of-friends halo finder to the distribution of DM particles, with a linking length equal to 0.15 times their mean separation. For each group of linked particles, we identify the particle having the minimum value of the gravitational potential. This particle is then used as the center of the cluster to run a spherical overdensity algorithm, which determines the radius around the target particle that encompasses a given overdensity. In the following analysis, we will consider a typical overdensity with respect to the critical density estimated at redshift z , $\rho_{c,z} = 3H_z^2 / (8\pi G)$, of $\Delta_z = 500 \times \Delta_{c,z} / \Delta_{c,EdS}$, where $\Delta_{c,z}$ is the ratio between virial and critical overdensity at redshift z for our cosmological model, while $\Delta_{c,EdS}$ is the same quantity in an Einstein–de-Sitter cosmology. This overdensity is chosen for convenience, since the regions within these overdensities are the most well-studied ones from an observational point of view (e.g. Ettori et al. 2004). Hereafter, we indicate by “ $\Delta = 500$ ” the cluster regions enclosed within a sphere with radius R_{500} and total gravitating mass

$$M_{500} = \frac{4}{3} \pi \rho_{c,z} \Delta_z R_{500}^3. \quad (1)$$

We measure, on average, R_{500} to be 0.63 times R_{vir} and constant

¹ <http://www.mpa-garching.mpg.de/gadget>

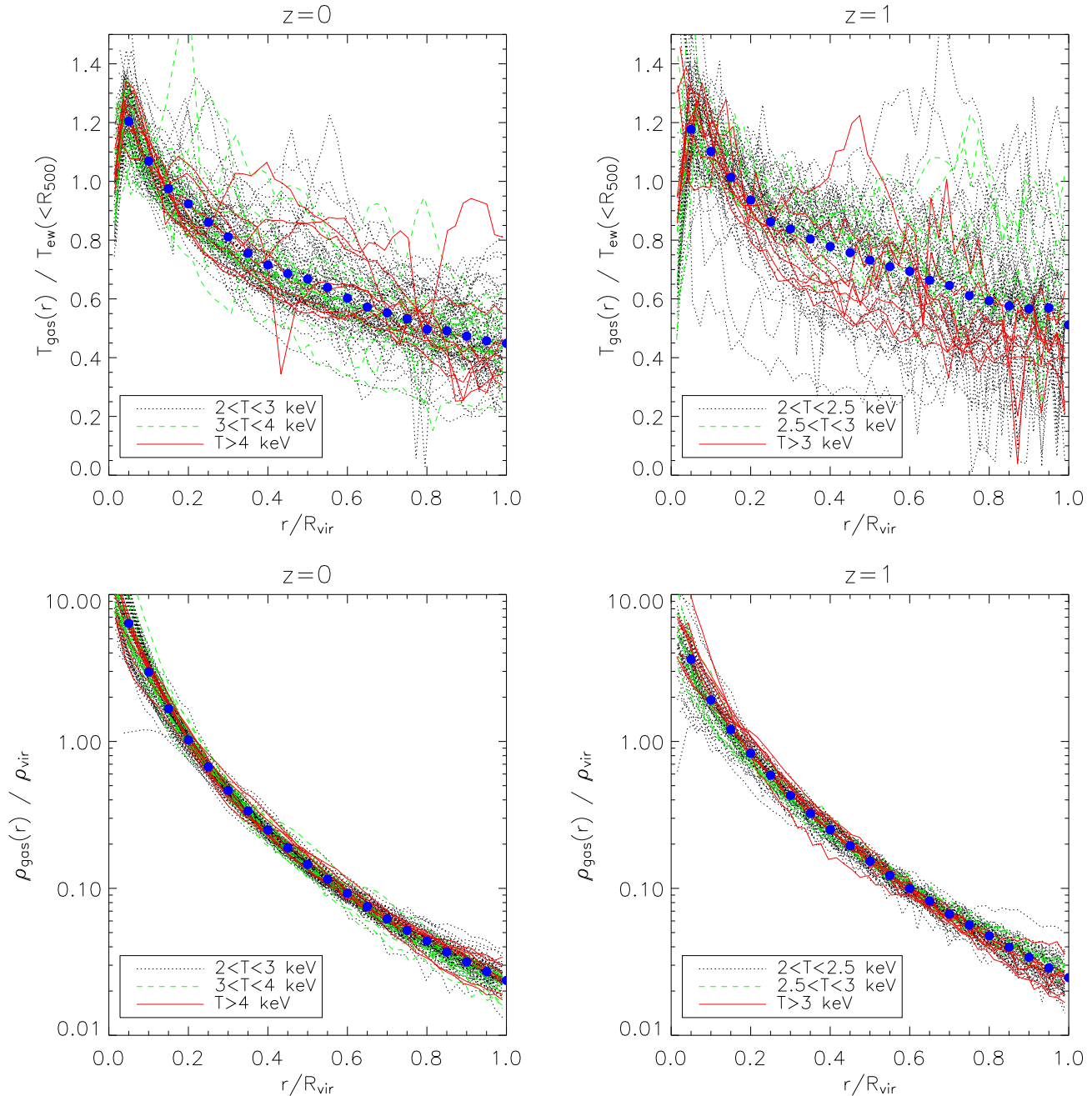


Figure 2. All (*lines*) and average (*dots*) differential 3-D gas temperature (upper panels) and density (lower panels) profile at redshift 0 (panels on the left) and 1 (panels on the right). The gas density is normalized to the virial value, ρ_{vir} , that is defined as the mean density within R_{vir} and is equal to $\rho_{c,z} \times \Delta_z$.

in redshift (we define R_{vir} as the radius encompassing an average density equal to the virial density for our cosmology and at a given redshift; e.g., Eke et al. 1996, Bryan & Norman 1998). This confirms that a fixed fraction of the virial radius is mapped by using the approximation to the solution for the collapse of a spherical top-hat perturbation. It is worth noticing that if one fixes the overdensity independently of the cosmological parameters and redshift, larger portion of the virial regions are mapped at higher redshift, since dark matter halos are more concentrated (i.e. have lower radial radius). E.g., assuming $\Delta_z = 500$, one obtains $R_{500}/R_{\text{vir}} = 0.49$, 0.56 and 0.58 at redshift 0, 0.5 and 1, respectively.

As we show in Paper I and discuss further below in this section, the simulated gas temperature and density profiles present clear deviations from the mean behaviour of the observed ones. Therefore, we decide to adopt the mass as defined in equation 1 and inferred from the simulated dark matter halos, instead of the corresponding value measured, e.g., through the hydrostatic equilibrium. We have measured, however, the reconstructed mass estimates at R_{500} by using an isothermal β -model (Cavaliere & Fusco-Femiano 1976) with a single emission-weighted temperature and inferring R_{500} from the corresponding mass profile (this procedure follows very closely what is generally done with obser-

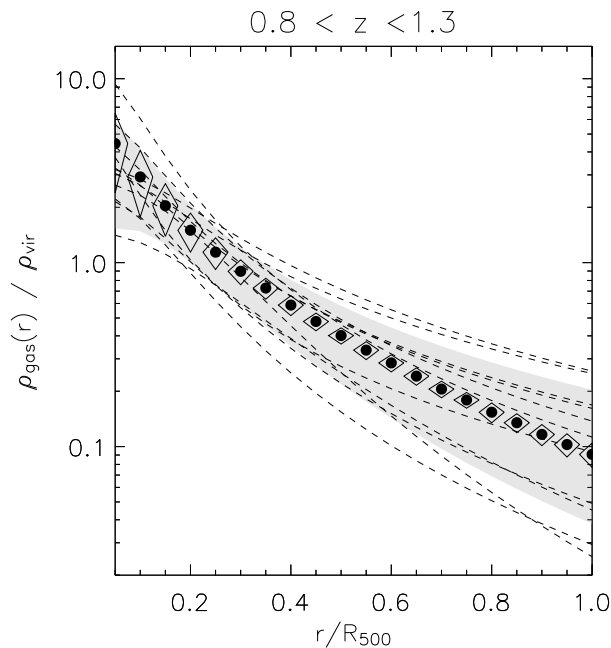


Figure 3. Gas density profiles at high redshift as function of r/R_{500} . *Dashed lines:* best-fit profiles from the *Chandra* exposures of the 11 galaxy clusters with $z > 0.8$ (Ettori et al. 2004). *Shaded region:* $(-1, +1)\sigma$ range around the mean value of the 11 observed profiles. *Dots:* average (plotted here with the corresponding dispersion) of the simulated density profiles at redshift 1 (see the right lower panel in Fig. 2).

Table 1. Distribution of the baryons in the selected sample of simulated galaxy clusters. The mean values of the indicated ratios are quoted.

z	n.obj	$\frac{M_{\text{neut}}}{M_{\text{bar}}}$	$\frac{M_{\text{star}}}{M_{\text{bar}}}$	$\frac{M_{\text{gas}}}{M_{\text{bar}}}$	$\frac{M_{\text{bar}}}{(\Omega_b/\Omega_m)}$
0	97	0.007	0.194	0.799	0.930
0.5	83	0.015	0.198	0.787	0.944
0.7	81	0.021	0.201	0.779	0.949
1	72	0.031	0.207	0.761	0.944

vational data, e.g. Ettori et al. 2004). It is worth noticing that the mass profile is then a direct function of the best-fit modelization of the gas density profile that, as we discuss at the end of this section, shows evident mismatches with what is typically observed. We obtain that the β -model estimates underestimate the true cluster mass by about 15 per cent on average at $z = 0$ and are in good agreement at $z = 1$ even though with a larger dispersion around the mean value of the distribution of the relative deviations (see Fig. 1). More relevant to the aim of this work is to note that these different definitions of the total gravitating mass, M_{tot} , do not affect significantly our results on the behaviour of the scaling relations. We refer to a forthcoming work in which the mass estimators applied to simulated and observed data will be discussed in detail (see also Rasia et al. 2004).

According to the multi-phase model, each gas particle of sufficiently high overdensity is assumed to be composed of a hot ionized phase and of a cold neutral phase, whose relative amounts depend on the local conditions of density and temperature (Springel

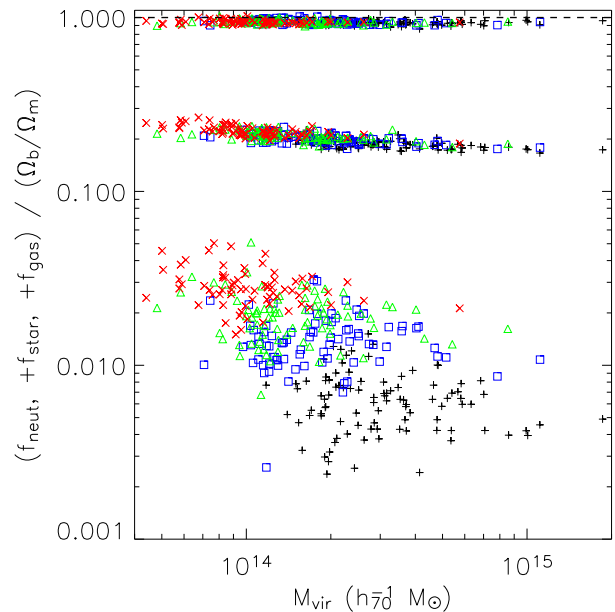


Figure 4. Distribution of the different components of the baryonic budget within the cluster virial radius as a function of the total mass. The three concentrations of points correspond to (from the bottom to the top) f_{neut} (~ 2 per cent), $f_{\text{neut}} + f_{\text{star}} = f_{\text{cold}}$ (about 20 per cent) and $f_{\text{cold}} + f_{\text{gas}}$ (95 per cent) in unit of the cosmic baryon value Ω_b/Ω_m . Each component f_i is equal to M_i/M_{vir} . The *plus* symbols are for the $z = 0$ objects, the *squares* for $z = 0.5$, the *triangles* for $z = 0.7$ and the *crosses* for $z = 1$.

& Hernquist 2003). By its nature, the neutral cold component is assumed not to emit any X-rays. Following Croft et al. (2001), we also exclude those particles from the computation of X-ray emissivity having temperature below 3×10^4 K and gas density $> 500\bar{\rho}_{\text{bar}}$, being $\bar{\rho}_{\text{bar}}$ the mean baryon density. In the following, we refer to *cold* gas as the gas which does not contribute to the X-ray emission and we distinguish it between a gas in a cold neutral phase, *neut*, and *stars*.

The X-ray luminosity of each cluster in a given energy band is defined as

$$L_X = (\mu m_p)^{-2} \sum_i^{N_{\text{gas}}} m_{h,i} \rho_{h,i} \Lambda(E_1, E_2; T_i), \quad (2)$$

where $\Lambda(E_1, E_2; T)$ is the cooling function in the energy band $[E_1, E_2]$. In this equation the sum runs over all N_{gas} gas particles falling within the cluster selected region, and μ is the mean molecular weight ($= 0.6$ for a gas of primordial composition), m_p is the proton mass, $m_{h,i}$ and $\rho_{h,i}$ are the mass and the density associated with the hot phase of the i -th gas particle, respectively. The cooling function is computed from a Raymond–Smith code (Raymond & Smith 1977) by assuming zero metallicity. For the purpose of comparing with observational results on the scaling relations, in the following luminosities are always given in the bolometric band. We define the emission-weighted temperature, T_{ew} , as

$$T_{\text{ew}} = \frac{\sum_i^{N_{\text{gas}}} m_{h,i} \rho_{h,i} \Lambda(E_1, E_2; T_i) T_i}{\sum_i^{N_{\text{gas}}} m_{h,i} \rho_{h,i} \Lambda(E_1, E_2; T_i)}. \quad (3)$$

We take $E_1 = 0.5(1+z)$ keV and $E_2 = 10(1+z)$ keV so as to reproduce the observational procedure in the estimate of the tem-

perature from the measured photon spectrum, whose reconstruction at low energies, say below 0.5 keV, is made hard by instrumental limitations. Notice however that, using simulated Chandra observations of galaxy clusters obtained with the software package X-MAS (X-ray MAP Simulator), Gardini et al. (2004) showed that the emission-weighted temperature inferred from hydrodynamical simulations can be significantly higher than the spectroscopic value extracted from observations (see also Mathiesen & Evrard 2001; Mazzotta et al. 2004).

Finally, we define the entropy of the i -th gas particle as $s_i = T_i/n_{i,e}^{2/3}$ where $n_{i,e}$ is the number density of free electrons associated to that gas particle.

Out of the ensemble of simulated bound structures, we analyse the 97, 83, 81 and 72 systems at redshift 0, 0.5, 0.7 and 1, respectively, that have an emission weighted gas temperature, T_{ew} , within $\Delta = 500$ larger than 2 keV. This selection allows to consider only the objects where the gravitational collapse dominates the energetic budget and that present a local temperature function and luminosity–temperature relation in good agreement with the observed ones (see Paper I).

In Figure 2, we plot the gas temperature and density profiles of the examined clusters at redshift 0 and 1. At higher redshift, (i) the radial profiles tend to be more spread around the mean value, suggesting that many systems are still in formation, (ii) the temperature distribution appears slightly flatter within the virial radius, decreasing by about 50 per cent from $0.2 \times R_{vir}$ to $0.8 \times R_{vir}$ (to be compared with a reduction by ~ 60 per cent at $z = 0$), and (iii) the central ($r < 0.2 \times R_{vir}$) gas density is less peaked by about 50 per cent than what observed at $z = 0$. However, the mean polytropic index γ , measured as the coefficient of the linear fit $\log T_{gas}(r) = k + (\gamma - 1) \times \log \rho_{gas}(r)$, remains almost constant with redshift, varying from 1.18 (rms: 0.04) at $z = 0$ to 1.16 (rms: 0.06) at $z = 1$. We conclude that the overall shape of the gas temperature and density profiles does not change significantly with redshift, even though local radial variations are present as a consequence of the different dynamical state of the objects, with dynamically younger systems being located at higher redshift.

In Figure 3 we show the comparison between simulated and observed gas density profiles at $0.8 < z < 1.3$. The observed profiles are recovered from the best-fit results obtained by applying a β -model to deep *Chandra* exposures (Ettori et al. 2004) and are normalized by the corresponding ρ_{vir} (see caption in Fig. 2) as done for simulated profiles. The overall shape seems in good agreement with the mean estimated values, even though the scatter in the observed data (indicated by the gray region in Fig. 3) is definitely larger than what is measured in the simulated ones at $z = 1$. This suggests that either the real data at high- z are subjected to a more complicated dynamical history than actually simulated or the latter ones are more regular due to the criteria adopted in selecting the dark matter halos. In detail, the more significant deviations are within $0.1 \times R_{500}$ and above $0.7 \times R_{500}$, where the steeper simulated profiles have mean values higher by 10–20 per cent and lower by 20 per cent (by 25 per cent at R_{500}) than the observed ones, respectively. The difference remains within few per cent in the range $(0.1 - 0.7) \times R_{500}$. On the other hand, once we limit our analysis to the hottest systems by selecting the 10 objects with the highest $T_{ew}(< R_{500})$, the discrepancy between the average profiles becomes more noticeable: deviations larger than 10 per cent are present within $0.4 \times R_{500}$ and beyond $0.8 \times R_{500}$. However, once we compare the rough estimate of the expected mean gas mass by integrating these average profiles over the cluster volume up to R_{500} , we obtain a reasonable agreement between the observed and

simulated values when only the hottest systems are analysed. A lower estimate by about 10 per cent is measured when the average gas density profile is obtained from all the simulated $z = 1$ objects.

The few observational data available on the gas temperature profiles at high- z (e.g. Jeltema et al. 2001, Arnaud et al. 2002) indicate isothermality up to half the virial radius but with typical relative uncertainties of 20 per cent or more (90 per cent confidence level) on each temperature measurement of the 3–4 radial bins. Mismatches between observed and simulated temperature profiles of the same order as highlighted in Paper I for local systems are probably present here but can not be confirmed. We refer the reader to section 3.3 and 3.4 of that paper for a detailed discussion of these discrepancies.

3 THE DISTRIBUTION OF BARYONS

The distribution of the baryons, and of the hot X-ray emitting gas in particular, is a diagnostic of the energetic phenomena that take place during the formation and evolution of galaxy clusters. Since this distribution affects the estimates of the gas density, entropy and emissivity, the analysis of how baryons populate the cluster potential well provides information on the properties of the integrated measurements.

Overall, we find between 1 (at redshift 0) and 3 (at $z = 1$) per cent of the baryons to be present in the cold phase, about 20 per cent in stars and between 77 (at $z = 1$) and 80 (at $z = 0$) per cent in the hot, X-ray emitting plasma. We also note a slight decrease from 7 to 5 per cent in the depletion of the baryons with respect to the assumed cosmic baryonic budget from $z = 0$ to 1 (see Table 1). These values of depletion, that have to be considered as lower limits considering the measured over-production of stars, are however comparable to what predicted from adiabatic simulations such as the ones considered in the Santa Barbara Project (Frenk et al. 1999) that indicate a mean $f_b/(\Omega_b/\Omega_m)$ of 0.92 (rms: 0.06).

The overall amount of cold gas, $M_{neut} + M_{star}$ is mainly composed of stars formed in high density regions and accounts for about 20 per cent of the total baryon budget (see average value in our samples in Table 1), at variance with a ~ 10 per cent estimate observed in nearby clusters (e.g. Lin et al. 2003). We point out that the major part of the star overproduction in simulated clusters takes place in the central cD galaxy, where the action of the galactic winds is not efficient enough to prevent overcooling. The lack of observational evidence for low-temperature gas in central cluster regions (e.g., Peterson et al. 2003) calls for the need of a central heating mechanism. We argue that this mechanism, which is not included in the present simulations, should reduce the resulting amount of stars. Moreover, there is a mild evidence for a higher efficiency to form stars in smaller systems (a trend also found in observations, see Fig. 7 in Lin et al. 2003) and at higher redshift (Fig. 4). As Springel & Hernquist (2003) suggest, this is an evidence for a less efficient formation of cooling flows in halos with virial temperature above 10^7 K. However, an analysis of our simulated clusters (Murante et al. 2004) shows that we have a diffuse star component, not associated with any galaxy, whose mass ranges from 10 per cent to more than 40 per cent of the total stellar mass of the cluster, being higher for more massive objects. Thus, the disagreement between the amount of cold baryons present in simulations and those observed could be lessened. Furthermore, depending on the spatial distribution of the diffuse component, the estimates of the star formation efficiencies could be slightly biased both in observations

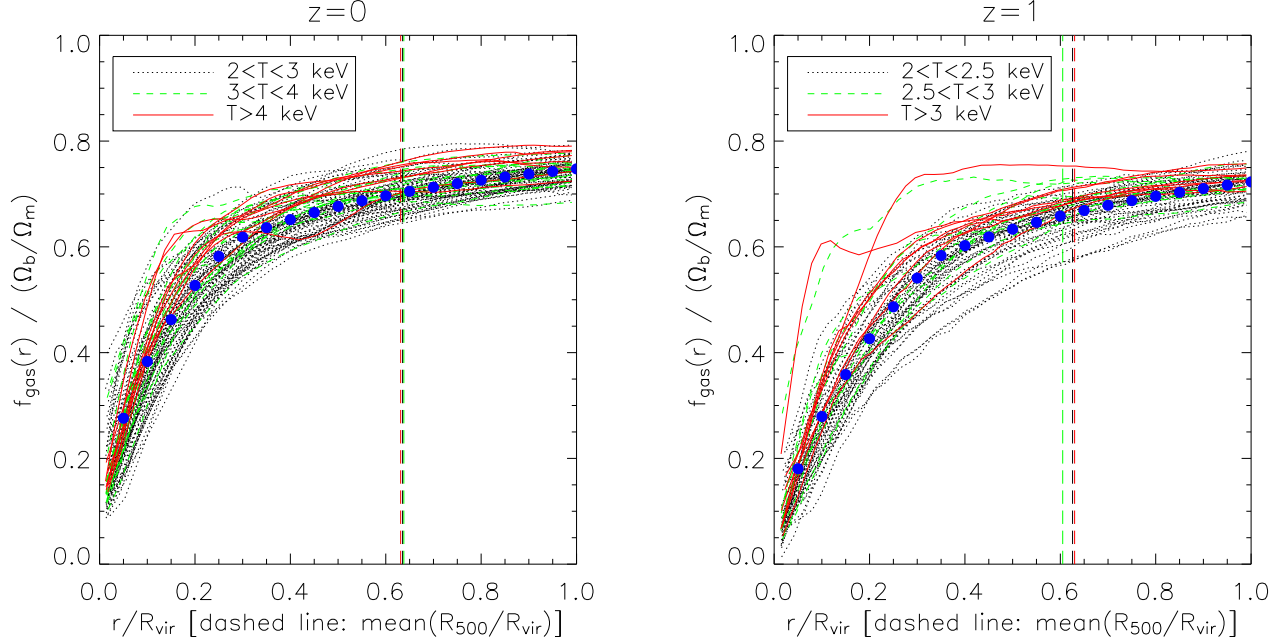


Figure 5. The gas fraction as a function of the radius in simulated clusters at $z = 0$ (left) and $z = 1$ (right). The *dots* represent the best-fit obtained by using the functional form in equation 4.

and in simulations, in the direction of having a smaller efficiency for massive clusters.

The X-ray emitting gas fraction, $f_{\text{gas}}(< r) = M_{\text{gas}}(< r)/M_{\text{tot}}(< r)$, increases when moving outward to $(0.3 - 0.4) \times R_{\text{vir}}$ and flattens then toward a constant value that is about $0.8 \times f_{\text{bar}} \approx 0.75 \times \Omega_b/\Omega_m$ (Fig. 5). This confirms that the hot ICM is more extended than the dark matter distribution, as already known from observational data (e.g. David et al. 1995, Ettori & Fabian 1999), and that one needs to sample the cluster X-ray emission out to $\sim 0.4 \times R_{\text{vir}} \approx 0.7 \times R_{500}$ to fully recover the baryon fraction in the form of hot plasma.

We find that a simple functional form can reproduce this dependence upon the radius quite well in the regions beyond the inner steep gradient, $f_{\text{gas}}(< r) \propto (2r)^\eta / (R_{\text{vir}} + r)^\eta$, with η about 0.2–0.3, whereas a further suppression is required to reproduce the profile within $\sim 0.3 \times R_{\text{vir}}$:

$$\frac{f_{\text{gas}}(< r)}{f_{\text{gas}}(< R_{\text{vir}})} = \min\left(\frac{r}{r_s}, 1\right)^\eta \times \left(\frac{2r/R_{\text{vir}}}{1+r/R_{\text{vir}}}\right)^\eta, \quad (4)$$

with $r_s \approx 0.3R_{\text{vir}}$. The best-fit results obtained by applying this functional form to the average radial profile of f_{gas} are: $f_{\text{gas}}(< R_{\text{vir}}) = 0.75 \times (\Omega_b/\Omega_m)$, η between 0.24 and 0.32, and r_s increasing from $0.28R_{\text{vir}}$ to $0.34R_{\text{vir}}$ when systems at higher redshift are considered.

To explore the gas mass fraction as a function of radius in the hottest systems that are more accessible to the observational analysis, we select the 10 hottest systems at redshift 0 and 1 (average value of $T_{\text{ew}}(< R_{500}) = 4.8$ and 3.4 keV, respectively). We measure then a mean (standard deviation) $f_{\text{gas}}/(\Omega_b/\Omega_m)$ of 0.638 (0.030) and 0.567 (0.071) at $R_{2500} \approx 0.28R_{\text{vir}}$, 0.732 (0.020) and 0.698 (0.026) at R_{500} , 0.760 (0.021) and 0.731 (0.015) within R_{vir} . Even though a larger contribution of hot gas to the cosmic fraction is measured at higher redshift, these measurements are in reasonable agreement once the associated scatter is considered.

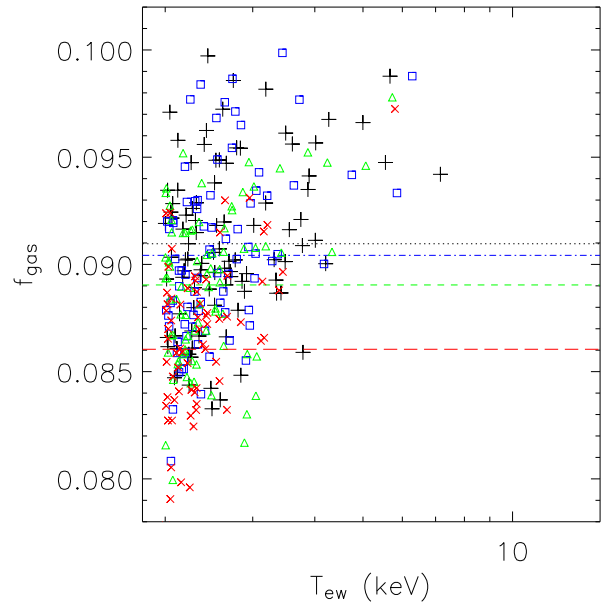


Figure 6. The gas fraction within $\Delta = 500$ as a function of the gas temperature. The symbols of the points are as in caption of Fig. 4. The horizontal lines indicate the mean values of the gas fraction at different redshift (*dotted line*: $z = 0$; *dash-dotted line*: $z = 0.5$; *dashed line*: $z = 0.7$; *long dashes*: $z = 1$).

4 THE SCALING RELATIONS AND THEIR EVOLUTION

Under the assumptions that the smooth and spherically symmetric intra-cluster medium (ICM) emits by bremsstrahlung and is in hydrostatic equilibrium with the underlying dark matter po-

Table 2. Best-fit results on the local ($z = 0$) scaling relations (dashed and dotted lines in the plots; see equation 5) of simulated galaxy clusters. The temperature, T , is in unit of 6 keV; the bolometric luminosity, L , in 10^{44} erg s $^{-1}$; the total mass, M_{tot} , in $10^{14} M_{\odot}$; the gas mass, M_{gas} , in $10^{13} M_{\odot}$. All these quantities are estimated within R_{500} . The entropy, S , is in unit of keV cm $^{-2}$ and is measured at $0.1 \times R_{200}$. When the slope A is fixed, we estimate the error-weighted mean of $(\log Y - A \log X)$ and evaluate the error after resampling Y and X by 1 000 times according to their uncertainties. The best-fit on the evolution parameter B (see equation 6) is obtained by considering (i) all the objects at redshift ≥ 0.5 , (ii) those at ≥ 0.7 and (iii) only the clusters at $z = 1$. The quoted errors are at 1σ level (68.3 per cent level of confidence and $\Delta\chi^2 = 1$ for one interesting parameter).

relation ($Y - X$)	α	A	$B (z \geq 0.5)$	$B (z \geq 0.7)$	$B (z = 1)$
$F_z M_{\text{tot}} - T$	1.07(± 0.06) 0.87(± 0.01)	2.08(± 0.15) 1.50 (fixed)	-0.12(± 0.05) -0.20(± 0.04)	-0.14(± 0.05) -0.22(± 0.04)	-0.20(± 0.07) -0.30(± 0.05)
$F_z M_{\text{gas}} - T$	1.14(± 0.08) 0.83(± 0.01)	2.40(± 0.20) 1.50 (fixed)	-0.12(± 0.05) -0.26(± 0.03)	-0.14(± 0.06) -0.30(± 0.03)	-0.22(± 0.08) -0.38(± 0.04)
$F_z^{-1} L - T$	1.23(± 0.14) 0.76(± 0.01)	3.33(± 0.35) 2.00 (fixed)	-0.76(± 0.08) -0.96(± 0.04)	-0.76(± 0.09) -0.98(± 0.04)	-0.80(± 0.11) -1.04(± 0.05)
$F_z^{-1} L - F_z M_{\text{tot}}$	-0.47(± 0.04) -0.39(± 0.02)	1.57(± 0.11) 1.33 (fixed)	-0.56(± 0.05) -0.68(± 0.04)	-0.56(± 0.05) -0.66(± 0.04)	-0.50(± 0.07) -0.64(± 0.05)
$F_z^{-1} L - F_z M_{\text{gas}}$	-0.35(± 0.03) -0.34(± 0.01)	1.38(± 0.07) 1.33 (fixed)	-0.58(± 0.03) -0.60(± 0.02)	-0.56(± 0.03) -0.58(± 0.03)	-0.50(± 0.04) -0.54(± 0.04)
$f_{\text{gas}} - T$	-1.01(± 0.01) -1.04(± 0.01)	0.09(± 0.02) 0.00 (fixed)	-0.04(± 0.03) -0.06(± 0.03)	-0.06(± 0.04) -0.06(± 0.04)	-0.08(± 0.05) -0.08(± 0.04)
$F_z^{4/3} S - T$	2.81(± 0.06) 2.66(± 0.01)	1.42(± 0.17) 1.00 (fixed)	0.26(± 0.04) 0.22(± 0.02)	0.24(± 0.04) 0.18(± 0.02)	0.18(± 0.05) 0.12(± 0.03)

tential, one can relate the bolometric luminosity, L , gas temperature, T , gas entropy, S , gas mass, M_{gas} , and total mass, M_{tot} in a simple and straightforward way. For instance, the equation of hydrostatic equilibrium, $d(\rho_{\text{gas}} T)/dr \approx \rho_{\text{gas}} GM_{\text{tot}}/r^2$, allows to write $M_{\text{tot}} \propto TR$ that, once combined with the definition of the total mass within a given overdensity Δ_z , $M_{\text{tot}} \propto E_z^2 \Delta_z R^3$, implies $E_z \Delta_z^{1/2} M_{\text{tot}} \propto T^{3/2}$, where $E_z = H_z/H_0 = [\Omega_m(1+z)^3 + 1 - \Omega_m]^{1/2}$ (for a flat cosmology with matter density Ω_m and Hubble constant at the present time H_0). Similarly, the definition of the bremsstrahlung emissivity $\epsilon \propto \Lambda(T)n_{\text{gas}}^2 \propto T^{1/2}n_{\text{gas}}^2$ (the latter being valid for systems sufficiently hot, e.g. > 2 keV) allows to relate the bolometric luminosity, L , and the gas temperature, T : $L \approx \epsilon R^3 \approx T^{1/2}n_{\text{gas}}^2 R^3 \approx T^{1/2}f_{\text{gas}}^2 M_{\text{tot}}^2 R^{-3} \approx f_{\text{gas}}^2 T^2$, where we have made use of the formula on the $M_{\text{tot}} - T$ relation shown above.

By combining these basic equations, we can obtain the scaling relations among the X-ray properties that we are going to investigate in the present section:

- $F_z M_{\text{tot}} \propto T^{3/2}$
- $F_z M_{\text{gas}} \propto T^{3/2}$
- $f_{\text{gas}} \propto T^0 \propto M_{\text{tot}}^0$
- $F_z^{-1} L \propto T^2$
- $F_z^{-1} L \propto (F_z M_{\text{tot}})^{4/3} \propto (F_z M_{\text{gas}})^{4/3}$
- $F_z^{4/3} S \propto T$,

where we have combined all the cosmological dependence in the factor $F_z = E_z \times (\Delta_z/\Delta_{z=0})^{1/2}$. All the quantities are measured within regions with overdensity $\Delta_z = 500$ (see Sect. 2), apart from the entropy S that is related to the thermodynamical entropy K ac-

cording to $K \propto \log S$, and is estimated as $T_{\text{gas}}(R_{0.1})/n_e^{2/3}(R_{0.1})$ with $R_{0.1} = 0.1 \times R_{200}$.

The relative error (at 1σ level of confidence) on the physical quantities is assumed to be 10 per cent for the luminosity, 15 per cent for the temperature and gas mass and 25 per cent for the gravitational mass. These uncertainties are the average values cited presently for local and high- z clusters (e.g. Finoguenov, Reiprich & Böhringer 2001, Ettori et al. 2004).

The behavior of these scaling laws are examined first in their normalization and slope by fitting the logarithmic relation

$$\log Y = \alpha + A \log X \quad (5)$$

between two sets of measured quantities $\{X_j\}$ and $\{Y_j\}$. We use the bisector modification (i.e. the best-fit results bisect those obtained from minimization in vertical and horizontal directions) of the linear regression algorithm in Akritas & Bershady (1996 and references therein, hereafter BCES for Bivariate Correlated Errors and intrinsic Scatter) that takes into account both any intrinsic scatter and errors on the two variables considered as symmetric. We adopt the best-fit results from the BCES($Y|X$) estimator only when the expected slope is zero, being the inverse one equals to infinity, like in the cases of the $f_{\text{gas}} - T$ relation. The uncertainties on the best-fit results are obtained from 10 000 bootstrap resampling.

With a relevant difference with respect to the analysis presented in Paper I, we have selected for the present analysis only galaxy clusters with $T_{\text{ew}}(R_{500}) > 2$ keV. Furthermore, because of the inclusion of a relative error on the measured quantities, the best-fit results do not necessarily coincide with those provided in Paper I. We refer to the latter work for a detailed discussion of the

Table 3. Best-fit results on the simulated and observed high- z ($z \geq 0.5$) samples. The relations and the parameters are defined in Table 2. The evolution parameter B is estimated by using the local relations indicated in Table 2 for simulated objects, and the best-fit values in Finoguenov et al. (2001, $M_{\text{tot}} - T$), Mohr et al. (1999, $M_{\text{gas}} - T$ and $f_{\text{gas}} - T$), Ettori et al. (2002, $L - T$), Reiprich & Böhringer (2002, $L - M_{\text{tot}}$) and Ponman et al. (2003, $S - T$) for the observed 22 clusters with $z \geq 0.5$ (Ettori et al. 2004). The deviations in σ between the parameter B as estimated in the simulations and observations are indicated in the column “ σ_B ”.

relation ($Y - X$)	α	A		B	α	A		B	σ_B
		from simulations				from observations			
$F_z M_{\text{tot}} - T$	1.29(± 0.12) 0.82(± 0.01)	2.72(± 0.31) 1.50 (fixed)	-0.12(± 0.05) -0.20(± 0.04)	0.85(± 0.04) 0.88(± 0.02)	1.89(± 0.45) 1.50 (fixed)	0.24(± 0.25)			-1.44
$F_z M_{\text{gas}} - T$	1.49(± 0.18) 0.83(± 0.01)	3.35(± 0.46) 1.50 (fixed)	-0.12(± 0.05) -0.26(± 0.03)	0.83(± 0.04) 0.98(± 0.02)	2.63(± 0.36) 1.50 (fixed)	-0.52(± 0.28)			1.42
$F_z^{-1} L - T$	1.45(± 0.22) 0.55(± 0.01)	4.33(± 0.54) 2.00 (fixed)	-0.76(± 0.08) -0.96(± 0.04)	0.58(± 0.07) 0.75(± 0.03)	4.12(± 0.75) 2.00 (fixed)	-2.20(± 0.46)			3.12
$F_z^{-1} L - F_z M_{\text{tot}}$	-0.61(± 0.02) -0.55(± 0.01)	1.57(± 0.07) 1.33 (fixed)	-0.56(± 0.05) -0.68(± 0.04)	-1.33(± 0.60) -0.38(± 0.04)	2.24(± 0.71) 1.33 (fixed)	-2.28(± 0.31)			5.44
$F_z^{-1} L - F_z M_{\text{gas}}$	-0.48(± 0.01) -0.48(± 0.01)	1.31(± 0.04) 1.33 (fixed)	-0.58(± 0.03) -0.60(± 0.02)	-0.70(± 0.06) -0.49(± 0.02)	1.55(± 0.07) 1.33 (fixed)	–			
$f_{\text{gas}} - T$	-0.96(± 0.03) -1.05(± 0.01)	0.24(± 0.09) 0.00 (fixed)	-0.04(± 0.03) -0.06(± 0.03)	-1.03(± 0.04) -0.89(± 0.02)	0.60(± 0.49) 0.00 (fixed)	-0.64(± 0.22)			2.75
$F_z^{4/3} S - T$	3.19(± 0.17) 2.71(± 0.01)	2.22(± 0.42) 1.00 (fixed)	0.26(± 0.04) 0.22(± 0.02)	2.75(± 0.02) 2.65(± 0.01)	0.70(± 0.23) 1.00 (fixed)	0.68(± 0.06)			-5.87

(mis)matches between observed and simulated scaling relations at $z = 0$. We concentrate here on the properties of these relations at high redshift ($z \geq 0.5$).

In the following sections, we discuss the slope, normalization and evolution with redshift of the power-law fit among these quantities and compare these results to the observational constraints obtained by Ettori et al. (2004) for a sub-sample of 22 X-ray galaxy clusters at $z \geq 0.5$ observed on kpc scales through deep *Chandra* observations. It is worth mentioning that, in the present analysis, we adopt systematically the definitions and methods discussed there to study the behaviour of the scaling laws of X-ray galaxy clusters. The results on the best-fit normalization and slope for the local scaling laws here investigated are given in Table 2 and shown as dotted (when the slope is fixed to the value predicted by the above scaling relations) and dashed (when the slope is a free parameter) lines in Figures 7 – 12. In Table 3, a synoptic summary of the best-fit results obtained from samples of simulated and observed clusters at $z \geq 0.5$ is given, with an assessment on the deviation between the evolution parameter B (see Section 4.2) as measured in the simulations and from observational data.

4.1 On the slope and normalization of the scaling relations

We fit equation 5 to the quantities of the simulated clusters at $z = 0$ and quote the results in Table 2. Overall, we observe a slope steeper than predicted from self-similar model in the examined scaling laws, with $L - T$ (Fig. 7), $M_{\text{tot}} - T$ (Fig. 8) and $M_{\text{gas}} - T$ (Fig. 9) relations being the ones with deviations larger than 3σ (best-fit of $A = 3.3 \pm 0.3$, 2.1 ± 0.2 and 2.4 ± 0.2 , respectively), whereas $S - T$ (Fig. 12) deviates by about 2.5σ from the expected values

of $A = 1$, $L - M_{\text{tot}}$ by 2.2σ and $L - M_{\text{gas}}$ is consistent with the predicted slope of $4/3$.

About the normalization of these scaling relations at high redshift ($z \geq 0.5$) and how they compare to the observed estimates, we use the results by Ettori et al. (2004) once the slope is fixed to the expected value from simple gravitational collapse assumption. The simulated clusters present normalizations that are definitely lower than what is actually observed in the same redshift range (see Table 3): α is lower by 7 per cent in the $M_{\text{tot}} - T$ relation, 12 per cent in the $M_{\text{gas}} - T$ relation, 27 per cent in the $L - T$ relation, 45 per cent in the $L - M_{\text{tot}}$ relation, 18 per cent in the $f_{\text{gas}} - T$ relation and consistent within few per cent in the $S - T$ relation. One possible explanation for these lower normalizations is that the amount of the hot X-ray emitting plasma measured within R_{500} of simulated systems at $z \geq 0.5$ is smaller than the observed one. This deficiency in the density of cosmic baryons detectable as hot gas in hydrodynamical simulations of galaxy clusters might be complementary to the well-known “over-cooling” problem, where radiative cooling converts a too large fraction of cosmic baryons into collisionless stars (e.g. Sugihara & Ostriker 1998, Balogh et al. 2001, Borgani et al. 2002) if the local cooling time is not conveniently increased by some sort of feedback process. On the other hand, the good agreement in the $L - M_{\text{gas}}$ relation suggests that overestimates of the gas temperature and total mass with respect to what actually measured can affect our overall results. We have indeed verified that by reducing, for example, by ~ 15 per cent the simulated estimates of both T and M_{tot} provides a general good match between the normalizations of the scaling relations in the observed and simulated datasets. We refer to a future work where we will compare different definitions of gas temperatures, as inferred from simulations,

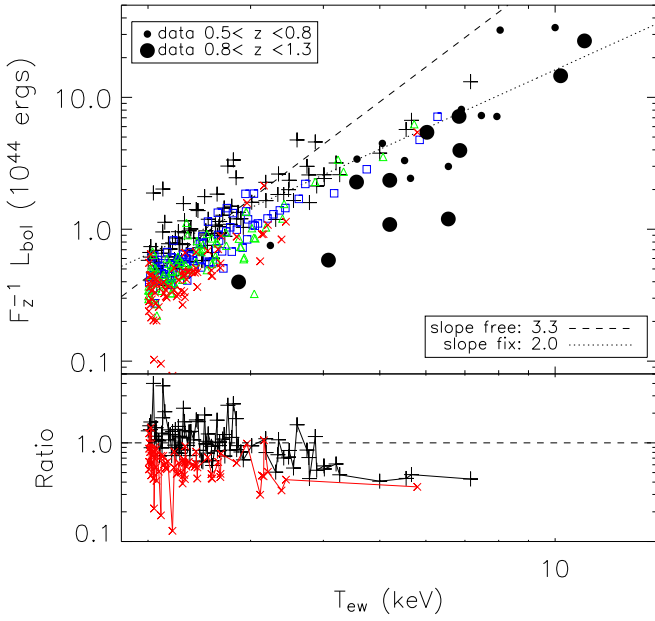


Figure 7. The local $L - T$ relation estimated at $\Delta = 500$ as best-fit from the simulated clusters at $z = 0$ (plus symbols). Dotted line: slope fixed to the predicted value. Dashed line: slope free. The simulated objects at $z = 0.5$ (squares), $z = 0.7$ (triangles) and $z = 1$ (crosses) are compared to the observed dataset from Ettori et al. (2004) with $0.5 < z < 0.8$ (small dots) and $z > 0.8$ (large dots). (**Lower panel**) Ratio between the measured luminosities at $z = 0$ (plus symbols) and $z = 1$ (crosses) and the best-fit local power-law.

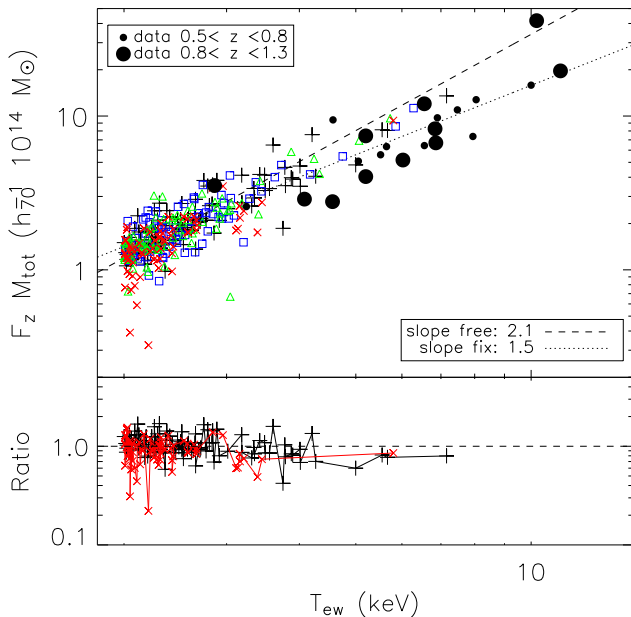


Figure 8. The same as in Fig.7, but for the $M_{\text{tot}} - T$ relation.

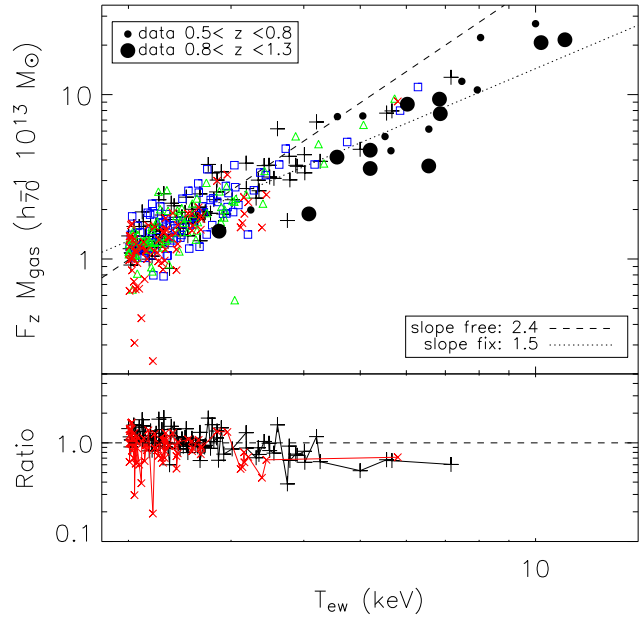


Figure 9. The same as in Fig.7, but for the $M_{\text{gas}} - T$ relation.

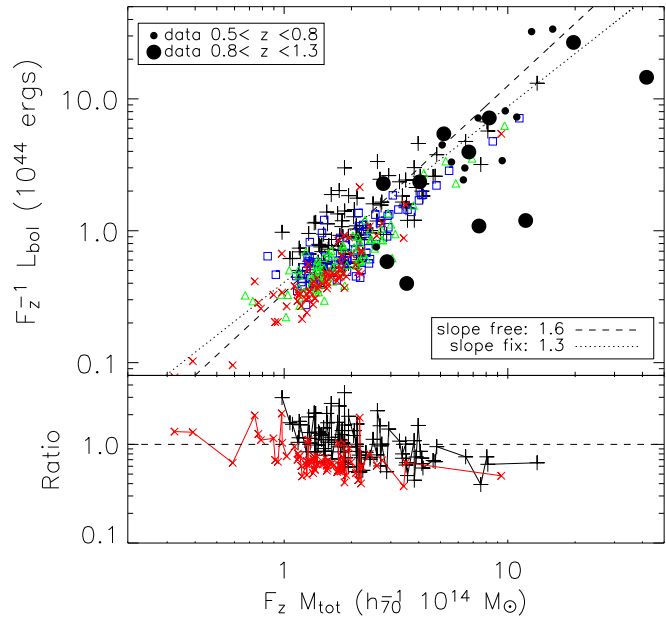


Figure 10. The same as in Fig.7, but for the $L - M_{\text{tot}}$ relation.

to observational data, and the implications on scaling relations and measurements of the cluster mass.

4.2 On the evolution of the scaling laws

We measure a median gas temperature of 2.5, 2.4, 2.3 and 2.3 keV in our samples at redshift of 0, 0.5, 0.7 and 1, respectively. On the other hand, we note a drastic decrease in the median values of $F_z^{-1} L / (10^{44} \text{ erg s}^{-1})$ from 1.01 at $z = 0$ to 0.61, 0.55 and 0.42 at

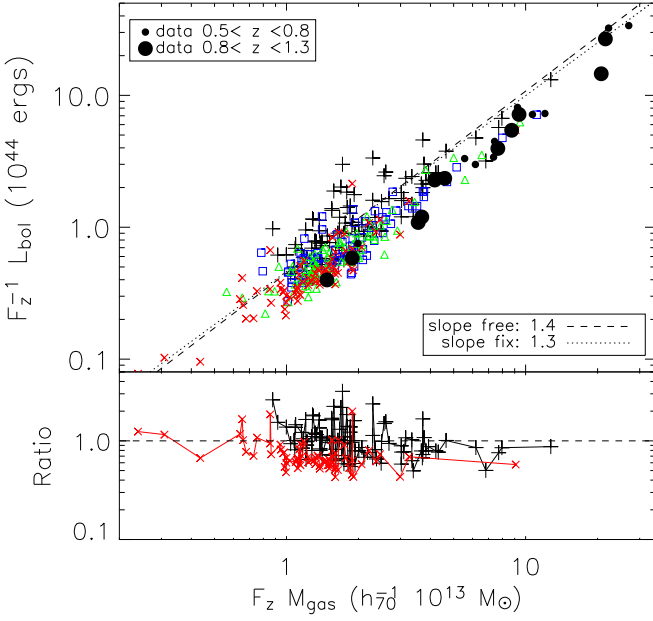


Figure 11. The same as in Fig.7, but for the $L - M_{\text{gas}}$ relation.

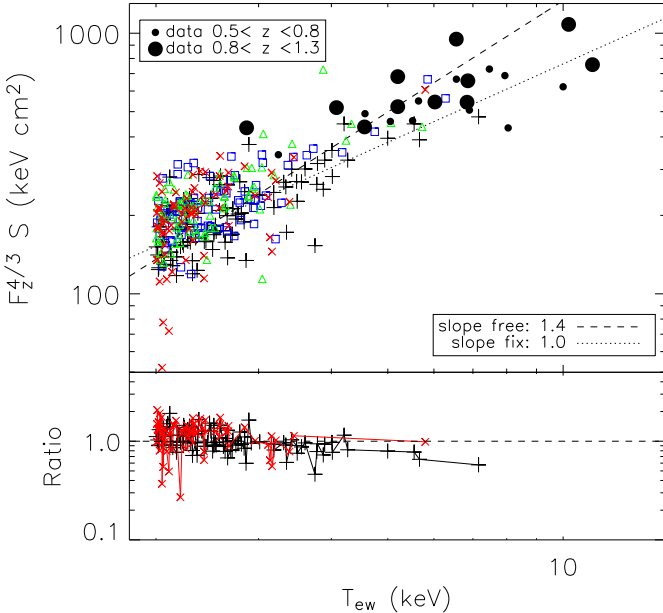


Figure 12. The same as in Fig.7, but for the $S - T$ relation evaluated at $R_{0.1} = 0.1 \times R_{200}$.

$z = 0.5, 0.7$ and 1 , mostly due to the cosmological correction introduced by the evolution of the Hubble constant and parametrized through E_z . Significantly lower values than those measured locally are also evaluated for the quantity $F_z M_{\text{tot}} / (10^{14} M_{\odot})$ that changes from 1.94 ($z = 0$) to 1.86 ($z = 0.5$), 1.63 ($z = 0.7$) and 1.53 ($z = 1$). These simple calculations give already indications for a declining luminosity and mass for given temperature and with in-

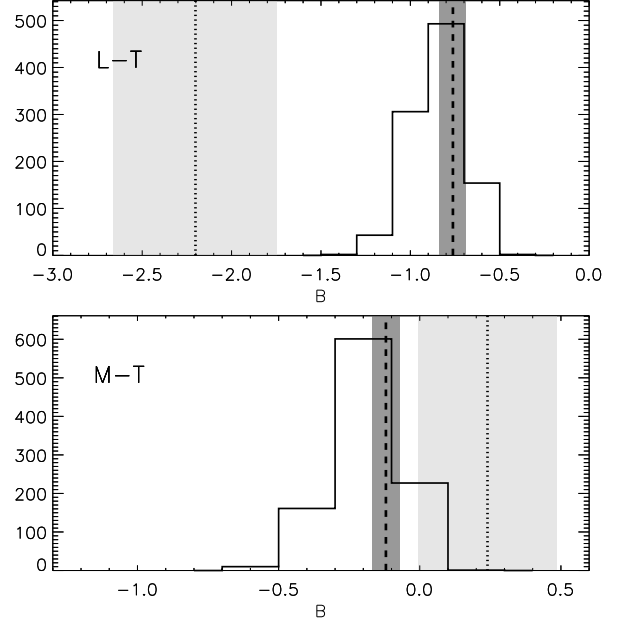


Figure 13. Distribution of the values of the evolution parameter B as measured in sub-samples of 22 simulated objects to mimic the dataset at $z \geq 0.5$ in Ettori et al. (2004). *Dark shaded region:* $1 - \sigma$ range and best-fit (*dashed line*) of B as evaluated for the overall sample of simulated clusters. *Light shaded region:* $1 - \sigma$ range and best-fit (*dotted line*) of B as evaluated in Ettori et al. (2004) for the same relation.

creasing redshift or, in other words, for a *negative* evolution of the corresponding scaling relations.

To constrain properly the evolution in the normalization of the considered scaling laws, we proceed as discussed in Ettori et al. (2004). First, we fix (α, A) to the best-fit results obtained from the clusters at $z = 0$, $(\bar{\alpha}, \bar{A})$, and, then, evaluate the confidence interval through a least-square minimization on the parameter B in the relation

$$\log Y = \bar{\alpha} + \bar{A} \log X + B \log(1 + z). \quad (6)$$

In particular, for a given grid of values of $\{B_i\}$, we search for the minimum of the merit function

$$\chi^2_i = \sum_j \frac{[\log Y_j - \bar{\alpha} - \bar{A} \log X_j - B_i \log(1 + z_j)]^2}{\epsilon_{\log Y_j}^2 + \epsilon_{\bar{\alpha}}^2 + \bar{A}^2 \epsilon_{\log X_j}^2 + \epsilon_A^2 \log^2 X_j}, \quad (7)$$

where the errors on the best-fit local values, $\epsilon_{\bar{\alpha}}$ and $\epsilon_{\bar{A}}$, are considered and propagated with the uncertainties, $\epsilon_{\log X} = \epsilon_X / (X \ln 10)$ and $\epsilon_{\log Y} = \epsilon_Y / (Y \ln 10)$, on the measured quantities.

We measure a small, but highly significant, *negative* (i.e. $B < 0$) evolution in the $L - T$ ($B \approx -0.8$) and $L - M_{\text{tot}}$ ($B \approx -0.6$) relations. Marginally ($< 3\sigma$) negative values of B are measured in the $M_{\text{tot}} - T$, $M_{\text{gas}} - T$ and $f_{\text{gas}} - T$ relations. A remarkable positive evolution is estimated in the $S - T$ relation. All these trends becomes more significant when objects at higher redshift are considered. In particular, the relative differences between local and $z = 1$ objects have been plotted in the lower panels of Figures 7 – 12, where the corresponding physical quantities are referred to the best-fit local power-laws. A clear segregation between local and high- z clusters is present in, e.g., the $L - T$ (Fig. 7) and $L - M_{\text{tot}}$ (Fig. 10) plots.

All these values in the evolution of the studied scaling relations are qualitatively consistent with the recent observational constraints (e.g. Ettori et al. 2004 and see Table 3). On the other side, the amount of measured evolution is less than actually observed in the simulated $L - T$, $L - M_{\text{tot}}$ and $S - T$ relations.

To check against any bias effect due to the number of objects selected in the sample, we have randomly extracted 7 objects at $z = 0.5$, 10 at $z = 0.7$ and 5 at $z = 1$ to mimic the distribution of the 22 observed clusters at $z \geq 0.5$ in Ettori et al. (2004) in which 7 clusters have redshift between 0.5 and 0.65, 10 are between $z = 0.65$ and $z = 0.85$ and 5 have z between 0.85 and 1.3. We have repeated the sampling for 1,000 times and plot the distribution of the values of the evolution parameter B in fig. 13. We conclude that no-significant deviations from the best-fit B value as measured for the overall sample are obtained when sub-samples are considered. Moreover, the observed evolution in the $L - T$ relation cannot be reproduced at very high significance (> 99.9 per cent), whereas the one observed in the $M_{\text{tot}} - T$ relation is only marginally consistent with the distribution of the B values (about 23 per cent of the simulated sub-samples have an evolution parameter that falls within the $1 - \sigma$ error range of the observed B value).

4.3 On the results obtained by adopting different selection criteria

We have repeated the analysis discussed above by extracting the simulated objects according to different criteria to answer two main issues:

(i). *What happens if we select only very massive systems (e.g. $T_{\text{ew}} > 3$ keV) in accordance to the observational datasets available?* By construction, no very massive virialized systems are build in this cosmological simulations implying that a selection at higher threshold in temperature (mass) reduces significantly the number of objects available. When we select the simulated clusters with $T_{\text{ew}} > 3$ keV, we collect just 24 objects at $z = 0$ and 8 at $z = 1$ (14 and 12 at $z = 0.5$ and 0.7 , respectively). Therefore, by decreasing the number of objects, we increase the statistical uncertainties of the best-fit parameters and no more significant evolution are detected. For example, in the $L - T$ relation we constrain the local slope to be 3.4 ± 1.6 , with a marginally negative evolution at $z \geq 0.5$ ($B \approx -0.7 \pm 0.4$). An evolution consistent with zero is measured in the $M_{\text{tot}} - T$ relation ($B = -0.1 \pm 0.3$ at $z \geq 0.5$), which presents a slope at $z = 0$ consistent with the predicted value of 1.5 (2.1 ± 1.1).

(ii). *How do the relations change when the gas mass-weighted temperature, T_{mw} , is used instead of the emission-weighted one (see, e.g., Allen et al. 2001, Thomas et al. 2002)?* If we select simulated clusters with $T_{\text{mw}} > 2$ keV, we reduce significantly the number of objects selected (42 vs. 97 simulated clusters at $z = 0$ and 12 vs. 72 at $z = 1$) and confirm by an indirect way the well-recognized problem of simulated cores being hotter than actually observed (see discussion on the temperature profile in section 3.4 in Paper I). All the scaling relations appear to be flatter and more consistent with self-similar predictions than measured when T_{ew} is in use: e.g., slopes of 3.0 ± 0.6 and 1.6 ± 0.2 are measured in the local $L - T$ and $M_{\text{tot}} - T$ relations. Also the evolution parameter B departs less significantly from zero, with values that are typically 50 per cent lower than the measured ones in the original selection.

5 SUMMARY AND DISCUSSION

Using a large cosmological hydrodynamical simulation, we have selected galaxy clusters at redshift $z = 0, 0.5, 0.7, 1$, all having T_{ew} within R_{500} larger than 2 keV, to explore the distribution of baryons and the X-ray scaling relations as function of redshift. We adopt an approach in our analysis that mimics observations, associating with each measurement an error comparable to recent observations and providing best-fit results obtained with robust techniques.

Our main findings can be summarized as follows:

(i). At $z \geq 0.5$, the simulated gas temperature and density profiles tend to show more scatter around the mean value, suggesting that many systems are still in formation and dynamically younger than the ones simulated locally. The temperature and density gradients are flatter and less centrally peaked, respectively, than those at $z = 0$. However, the overall shape of these radial profiles represented by the polytropic index does not change significantly.

(ii). Gas density profiles for simulated clusters are slightly steeper than actually observed at $z \approx 1$, with deviations of about 10-20 per cent (on average) below $0.1 \times R_{500}$ and above $0.7 \times R_{500}$. This implies a mean integrated value of the simulated gas mass lower by about 10 per cent. A significantly larger scatter in the observed data suggests that either the complex dynamical history of the formation of these structures is not recovered fully in this hydrodynamical simulation or the simulated dark matter halos are more regular due to the criteria adopted in their selection.

(iii). The baryons within the virial radius are distributed among a cold phase, with a relative contribution that increases from less than 1 to 3 per cent at higher redshift, a collisionless phase in stars of about 20 per cent and the X-ray emitting plasma that contributes by 80 (76) per cent at $z = 0(1)$ to the total baryonic budget. A depletion of cosmic baryons of the order of ~ 7 per cent is measured locally at the virial radius, R_{vir} . The average value of the depletion decreases slightly to 5 per cent at $z = 1$. These values are consistent with the results obtained in adiabatic hydrodynamical simulations, even though they have to be considered as lower limits considering the measured over-production of stars.

(iv). The X-ray emitting gas mass fraction, $f_{\text{gas}}(< r)$, increases with r as a power-law with a characteristic scale that also increases from 0.28 to $0.34 \times R_{\text{vir}}$ when going from $z = 0$ to $z = 1$, with a typical slope of about 0.25. The measured gas fraction in the ten hottest systems at R_{2500} , R_{500} and R_{vir} is 0.62, 0.73 and 0.76 $\times (\Omega_{\text{b}}/\Omega_{\text{m}})$ at $z = 0$ and 0.57, 0.70 and 0.73 $\times (\Omega_{\text{b}}/\Omega_{\text{m}})$ at $z = 1$, respectively. The differences as function of redshift are not significant being within the measured scatter.

(v). We confirm that, also at high- z , simulated clusters have X-ray scaling relations between temperature, T , luminosity, L , central entropy, S , gas mass, M_{gas} , and total gravitating mass, M_{tot} , which are steeper than predicted by simple gravitational heating.

(vi). When we fix the slope of these scaling laws to the values expected from the self-similar scenario, normalizations α lower by 10-40 per cent are measured in the $L - T$, $M_{\text{tot}} - T$, $M_{\text{gas}} - T$ and $L - M_{\text{tot}}$ relations at $z \geq 0.5$ when compared to the observational results for high redshift clusters (e.g. Ettori et al. 2004). The normalization of the central entropy - temperature relation is instead higher by few per cent, confirming the lack of gas mass in the central regions of these high- z simulated systems. On the other hand, the good agreement in the $L - M_{\text{gas}}$ relation suggests that overestimates of the gas temperature and total mass with respect to what actually measured can affect our overall results. We have indeed verified that by reducing by 15 per cent the simulated estimates of

both T and M_{tot} provides a general good match between the normalizations of the scaling relations in the observed and simulated clusters. In this perspective, it should be noticed that Mazzotta et al. (2004) have recently suggested a spectroscopic-like definition of the ICM temperature from simulations that better matches the temperature obtained from the spectral fit of observational data. This alternative definition tends to provide temperature estimates lower than the emission-weighted values when the thermal structure of the cluster in exam deviates more from an isothermal modelization.

(vii). We measure a declining luminosity and mass for given temperature and with increasing redshift. This *negative* evolution is parametrized through a power-law dependence upon the redshift, $(1+z)^B$, with $B \approx -0.8$ for the $L-T$ relation, $B \approx -0.2$ for the $M_{\text{tot}}-T$ relation, $B \approx -0.2$ for the $M_{\text{gas}}-T$ relation and $B \approx -0.6$ for the $L-M_{\text{tot}}$ and $L-M_{\text{gas}}$ relations. A slightly positive evolution of $B \approx +0.2$ is measured in the $S-T$ relation. As shown in Table 3, these results are consistent (deviation less than 3σ) with the observed evolution evaluated in a similar redshift range (e.g. Ettori et al. 2004) for the $M_{\text{tot}}-T$, $M_{\text{gas}}-T$ and $f_{\text{gas}}-T$ relations. Significantly less evident evolution are instead measured in the simulated $S-T$, $L-M_{\text{tot}}$ and $L-T$ relations. We have verified that the amount of evolution estimated here is robust against bias effects due to the number of objects examined.

Our results demonstrate that the present dataset of simulated galaxy clusters tends to evolve at higher redshift, with a flatter gas temperature profile and a less centrally peaked density profile and a statistically significant deficiency of X-ray emitting plasma (items i, iii, iv and vii above).

The comparison with the observational constraints at $z \geq 0.5$, performed by adopting the same definitions of the examined quantities and analyzing comparable samples both in size and physical properties, further indicates that the measured lower normalizations (item vi above) suggest either a significant lack of X-ray luminous baryons or an overestimates of the simulated values of the gas temperatures and total gravitating mass. An evolution toward less luminous and massive systems for given gas temperature at higher redshift (item vii) is measured in the simulated dataset in good agreement with recent observational results.

Overall, our results show how the study of the evolution in the scaling relations can give indications on the properties of the feedback that can be investigated through extensive hydrodynamical simulations. In particular, these results support the request for either more efficient feedback or extra physical processes, which are able to suppress (i) the over production of stars in the central cluster regions and (ii) the lack of cosmic baryons in the hot X-ray emitting phase. Moreover, this additional source of heating is required not only to provide extra energy but also to distribute it radially in such a way (iii) to improve the agreement between the simulated and observed gas temperature both locally and up to redshift of 1, (iv) to reduce the steepening of the gas density profile at high- z , (v) to ‘soften’ the gas density profiles of low temperature objects by increasing the central entropy, as already discussed in Paper I.

The work presented here demonstrates that we are approaching an age in which code efficiency and supercomputing capabilities make the simulations able to describe the formation and evolution of cosmic structures over a fairly large dynamical range in a fruitful symbiosis with the present observational limits. The real challenge for improving the exchange between numerical and observational cosmology is, on the one side, to build algorithms that more faithfully incorporate all those astrophysical processes

that are suspected to give relevant contribution to the observational properties of highly non-linear and over-dense structures, and on the other side, to resolve spatially with a sufficient number of photons even at $z \approx 1$ all the physical quantities of interest, starting with the temperature of the X-ray emitting plasma.

ACKNOWLEDGEMENTS

We thank the anonymous referee for helpful comments that improved the presentation of the work. The results presented in this paper are based on a simulation realized using the IBM-SP4 machine at the “Consorzio Interuniversitario del Nord-Est per il Calcolo Elettronico” (CINECA, Bologna), with CPU time assigned thanks to the INAF-CINECA numerical Key-Project “A *Tree+SPH High-Resolution Simulation of the Cosmic Web*” (2003). This work has been partially supported by the INFN-PD51 grant and by MIUR.

REFERENCES

- Akritas M.G., Bershadsky M.A., 1996, *ApJ*, 470, 706
 Allen S.W., Schmidt R.W., Fabian A.C., 2001, *MNRAS*, 328, L37
 Arnaud M. et al., 2002, *A&A*, 390, 27
 Balogh M.L., Pearce F.R., Bower R.G., Kay S.T., 2001, *MNRAS*, 326, 1228
 Borgani S., Governato F., Wadsley J., Menci N., Tozzi P., Quinn T., Stadel J., Lake G., 2002, *MNRAS*, 336, 409
 Borgani S., Murante G., Springel V., Diaferio A., Dolag K., Moscardini L., Tormen G., Tornatore L., Tozzi P., 2004, *MNRAS*, 348, 1078 (Paper I)
 Bryan G.L., Norman M.L., 1998, *ApJ*, 495, 80
 Cavaliere A., Fusco-Femiano R., 1976, *A&A*, 49, 137
 Croft R.A.C., Di Matteo T., Davé R., Hernquist L., Katz N., Fardal M.A., Weinberg D.H., 2001, *ApJ*, 557, 67
 David L.P., Jones C., Forman W., 1995, *ApJ*, 445, 578
 Eke V.R., Cole S., Frenk C.S., 1996, *MNRAS*, 282, 263
 Ettori S., Fabian A.C., 1999, *MNRAS*, 305, 834
 Ettori S., De Grandi S., Molendi S., 2002, *A&A*, 391, 841
 Ettori S., Tozzi P., Borgani S., Rosati P., 2004, *A&A*, 417, 13
 Evrard A.E., Henry J.P., 1991, *ApJ*, 383, 95
 Finoguenov A., Reiprich T.H., Böhringer H., 2001, *A&A*, 368, 749
 Frenk C. et al., 1999, *ApJ* 525, 554
 Gardini A., Rasia E., Mazzotta P., Tormen G., De Grandi S., Moscardini L., 2004, *MNRAS*, in press (astro-ph/0310844)
 Haardt F., Madau P., 1996, *ApJ*, 461, 20
 Holden B.P., Stanford S.A., Squires G.K., Rosati P., Tozzi P., Eisenhardt P., Spinrad H., 2002, *AJ*, 124, 33
 Jeltama T.E., Canizares C.C., Bautz M.W., Malm M.R., Donahue M., Garmire G.P., 2001, *ApJ*, 562, 124
 Kaiser N., 1986, *MNRAS*, 222, 323
 Kaiser N., 1991, *ApJ*, 383, 104
 Lin Y.T., Mohr J.J., Stanford S.A., 2003, *ApJ*, 591, 749
 Mathiesen B.F., Evrard A.E., 2001, *ApJ*, 546, 100
 Mazzotta P., Rasia E., Moscardini L., Tormen G., 2004, *MNRAS*, submitted (astro-ph/0404425)
 Mohr J.J., Mathiesen B., Evrard A.E., 1999, *ApJ*, 517, 627
 Murante G. et al., 2004, *ApJL*, 607, L83
 Peterson J.R., Kahn S.M., Paerels F.B.S., Kaastra J.S., Tamura T., Bleeker J.A.M., Ferrigno C., Jernigan J.G., 2003, *ApJ*, 590, 207
 Ponman T.J., Sanderson A.J.R., Finoguenov A., 2003, *MNRAS*, 343, 331
 Rasia E., Tormen G., Moscardini L., 2004, *MNRAS*, in press (astro-ph/0309405)
 Raymond J.C., Smith B.W., 1977, *ApJS*, 35, 419
 Reiprich T.H., Böhringer H., 2002, *ApJ*, 567, 716
 Springel V., Hernquist L., 2002, *MNRAS*, 333, 649
 Springel V., Hernquist L., 2003, *MNRAS*, 339, 289

- Springel V., Yoshida N., White S.D.M., 2001, *NewA*, 6, 79
Suginohara T., Ostriker J.P., 1998, *ApJ*, 507, 16
Thomas P.A., Muanwong O., Kay S.T., Liddle A.R., 2002, *MNRAS*, 330,
L48
Vikhlinin A., Van Speybroeck L., Markevitch M., Forman W.R., Grego L.,
2002, *ApJL*, 578, L107